

tmp title: MUSC source

Damien Pageot^{*†}, Donatienne Leparoux^{*}, Mathieu Le Feuvre^{*}, Olivier

Durand^{*} and Yann Capdeville[†]

^{*}*LUNAM-IFSTTAR*,

[†]*OSUNA*

^{*}*LPGN*,

(September 29, 2015)

GEO-Example

Running head: *Geophysics example*

ABSTRACT

INTRODUCTION

Since the early developments of seismic imaging methods in the middle of 20th century, approaches and algorithms innovations are still proposed in current research projects. The improvements deal with both the qualitative imaging techniques like migration (e.g. Berkhout et al. (2012); Guofeng et al. (2013)), novel applications of quantitative imaging methods such as the first arrival tomography (e.g. Bohm et al. (2015)), or even more recent approaches like the Full Waveform Inversion (e.g. Perez Solano et al. (2014), see Virieux and Operto (2009) for a revue of this last decade). The refinements are proposed for different scales like near surface applications for civil engineering topics or more deeper investigation for example for oil prospection or crustal imaging at regional or global scales They are mostly validated by using synthetic data, for example with well known shared benchmark (like the Marmousi case). However, the synthetic data are generally computed using the same wave propagation modeling engine used in the inverse problem process. In other terms, the synthetic data are computed with some assumptions which are the same in the inverse problem, for example the approximation of acoustic propagation, a 2D space medium, or a 2D line source. This approach, called *inverse crime* (Wirgin, 2004) is particularly useful for validating an algorithm in its early development stage but does not take into account the artefacts that can be due to the assumptions of the direct problem. Some authors tackle this issue by providing 3D data which are inverted with a 2D approach or other restrictive assumptions (e.g). But also in this case, the approach does not allow to assess the efficiency of the method for real seismic data. Moreover, because no one knows precisely the Earth interior, it is difficult to evaluate the capacity of a method to recover physical parameters and structures from real seismic data which can lead sometimes to geological misinterpretation due to numerical artifacts (Morozov, 2004). Thus, it is necessary to add

a step for which imaging methods will be tested for experimental seismic measurements
25 obtained under controlled conditions.

The best way to satisfy this need is to use Physical Small Scale Modeling Methods (noted
PSM subsequently). *PSM* were used since several years to study the propagation of waves
in various media with several stage of complexity, from acoustic wave propagation in homo-
geneous media to elastic wave propagation in three-dimensional heterogeneous anisotropic
30 media (Rieber, 1936; Howes et al., 1953; Hilterman, 1970; French, 1974; Bishop et al., 1985;
Pratt, 1999; Favretto-Cristini et al., 2013; Sarkar et al., 2003; Isaac and Lawton, 1999), and
allow to generate experimental seismic data under well-controlled conditions. In this way,
recent studies have been conducted to simulate multi-sources and multi-receivers through
piezzo-electric transducers (Wong et al., 2009). An alternative approach consists in using the
35 laser interferometry as the receiver system, as done in the MUSC Laboratory (Bretaudeau
et al., 2008, 2011, 2013), *Mesure Ultrasonore Sans Contact* in French, is one of them. This
technology, by avoiding the contact of the receivers on the model, allows to by-pass the
coupling issue of transducers that is difficult to model. In this way, the MUSC laboratory is
designed to simulate (1) wide-angle on-shore acquisitions modeling both body waves and sur-
40 face waves, (2) automatic multisource-multireceiver measurements with a high-productivity,
(3) high-precision source-receiver positioning and (4) high-precision recording of absolute
surface displacement without coupling effects.

Our objective here is to increase the potential of the MUSC system as a reliable tool for
generating experimental data which will be distributed in the scientific community. Thus,
45 we present two studies of experimental data in order to : 1) refine the comparison between
numerical and experimental data by taking into account the 3D/2D geometrical spreading
effects through an alternative way and 2) identify the reproducibility of the source impact

and, consequently, data repeatability. These approaches will complete the knowledge of the system and facilitate the achievement of massive multi-source and multi-receiver data
50 simulating subsurface seismic experimental campaigns.

To achieve some of these objectives, we used a seismic wave modeling code based on the Spectral Element Method (Komatitsch et al., 1998; Komatitsch and Tromp, 1999; Komatitsch et al., 2005; Festa and Vilotte, 2005). This method has several advantages compared to finite differences and finite elements, such as: (1) a weak formulation which can
55 naturally take into account the free surface, (2) an explicit scheme in time facilitating parallelization and reducing the computational cost, (3) a spatial discretization (mesh) convenient for the representation of complex environments and (4) high precision results and low numerical dispersion.

Thus, this article is organized as follow. In a first part, we present the MUSC laboratory
60 and the SEM code used for the studies. In a second part, we present two coupled studies of experimental data in order to: (1) refine the comparison between numerical and experimental data by taking into account the geometrical spreading effects between two-dimensional and three-dimensional data through an alternative way, and (2) identify the reproducibility of the source impact to validate the data reproducibility.

METHODS

65 **Physical modeling: MUSC system**

The MUSC system (Bretaudeau et al., 2008, 2011, 2013) is built to experimentally reproduce field seismic data with a great accuracy on small scale model. Figure 1 shows the bench and its components. MUSC system is composed of a honeycomb tab and two arms which

control the source and the receiver position with a precision of $10\text{ }\mu\text{m}$.

70 The receiving system of MUSC system is a laser interferometer. The principle of this laser is based on a phase shift of the reflected laser signal due to the wave propagation in the material. A real-time calibration value enables a continuous conversion to a nanometric displacement. The focal diameter of the laser on the model surface is about several micrometers and allows a detection limit of 2.5 nm (few) in the frequency range from 30 kHz 75 to 20 MHz .

The seismic source is simulated by a piezoelectric transducer relied to a launching and synchronization system. This system provides more energy than a laser impulse source (Bretaudeau, 2010; Bretaudeau et al., 2011) and allows to choose the source function, *i.e.*, Gauss source, Ricker source, central frequency f_0 and time delay t_0 . The source is generated 80 by a waveform generator and is then amplified before transmitted to the small-scale-model. In the framework of seismic physical modeling, the source must be as closed as possible to a normal point source. Thus, the piezoelectric source is coupled with an adapter in order to reproduce the spatial energy repartition (limiting directivity) and conserving the waveform as shown in figure 3.

85 For the purpose of small scale modeling, the change of scale must keep the relationship between observables. For most of seismic imaging methods, the significant physical parameters are the compressional and shear waves velocities, V_P and V_S respectively, the density ρ and the quality factor Q . When scaling the model, many parameters can be modified: the distances, the time scale, the amplitudes of the signals, the viscoelastic properties, etc. 90 Hence, the predominant factor is the wavelength $\lambda = V/f$, where V is the wave velocity and f the frequency. Thus, physical and mechanical parameters are modified to preserve the

ratio $\lambda_{real} = \xi \lambda_{scale}$ where ξ is the scale ratio. It is therefore necessary to act directly on the time-frequency scales. Assuming the materials used to build the small scale model have the same mechanical properties (V_P , V_S , ρ) than the natural media, it is straightforward to
95 obtain the scale ratios for parameters involved in seismic experiment.

For near surface experiments, the scale ratio ξ is about 1000 which means that the central frequency f_0 of the source is few kHz (generally 100 kHz but can be more or less), distances are in mm (acquisition length around 50 mm typically) and time unit is ms . (V_P , V_S etc...)

Small-scale models are generally made of metal, thermoplastic or melted epoxy resin-based
100 materials (Bretaudeau et al., 2013, 2011, 2008). These materials allow to reproduce complex geometries and have a large panel of physical and mechanical properties. These materials have the advantages to have physical properties closed to natural soil materials after scaling. The models are generally over-sized to easily separate reflected waves on boundaries from the rest of the signal.

105 Numerical modeling: Spectral Element Method

Various numerical methods exist to resolve the equation of motion in arbitrary elastic media. The most widely used is the Finite-Differences (FD) method (Virieux, 1986; Levander, 1988; Robertsson et al., 1994; Pratt, 1990; Stekl and Pratt, 1998; Saenger and Bohlen, 2004) which estimates each derivative on a regular Cartesian grid using a Taylor development (Moczo
110 et al., 2004) of order n . FD is simple to implement but quickly shows some limitations: the Cartesian grid is defined by the minimum propagated wavelength (λ_{min}) in the full media and is unable to reproduce properly complex topography and interfaces. Moreover, Saenger et al. (2000) show that 60 points by wavelength (λ) are needed to model propagation of

Rayleigh wave in order $n = 2$ where only 15 points by λ are required to model propagation of
115 body waves which increases drastically the numerical cost in case of near-surface modeling
experiment. The Finite-Elements Method (FEM) is another popular method used for wave
propagation modeling (Lysmer and Drake, 1972; Seron et al., 1990; Hulbert and Hughes,
1990). FEM is based on a variational formulation of the equation of motion and gives a
continuous approximate solution in space using polynomial basis functions defined on each
120 node of each cell of the mesh. The natural boundary conditions of FEM is the free surface
and the triangular (in 2D) or tetraedric (in 3D) unstructured meshes are well adapted to
complex media and topography. However, low polynomial basis are inadequate with fine
spatial discretization and the required discretization to obtain precise and non-dispersive
solution is numerically costly.

125 Recently, the Spectral Element Method (SEM), widely used in fluid dynamics (Patera, 1984;
Korczak and Patera, 1986; Karniadakis, 1989), was adapted to seismic wave propagation
(Komatitsch et al., 1998; Komatitsch and Tromp, 1999; Komatitsch et al., 2005; Festa and
Vilotte, 2005).

The SEM is based upon a high-order piecewise polynomial approximation of the weak
130 formulation of the wave equation. It combines the accuracy of the pseudo-spectral method
with the flexibility of the finite-element method (Tromp et al., 2008).

In this method, the wave-field is represented in terms of high-degree Lagrange interpolants,
and integrals are computed based upon Gauss-Lobatto-Legendre (gll) quadrature. This
combination leading to a perfectly diagonal mass matrix leads in turn to a fully explicit
135 time scheme which leads itself very well to numerical simulations on parallel computers. It
is particularly well suited to handling complex geometries and interface matching conditions

(Cristini and Komatitsch, 2012).

As in FEM, all boundary of the domain are reflecting and the free surface is the natural condition. In order to simulate infinite or semi-infinite domain, SEM can use Perfect Match
140 Layers boundary conditions (Bérenger, 1994; Festa and Vilotte, 2005) but are not used here.

The typical element size that is required to generate an accurate mesh is of the order of λ , λ being the smallest wavelength of waves traveling in the model.

Models are meshed in 2D with quadrangles using the open-source software package GMSH (Geuzaine and Remacle, 2009).

RESULTS

145 From point-source to line-source response

In the framework of wave propagation modeling and imaging methods, most of available algorithms are limited to the two-dimensional approximation especially for computational cost causes. More, a widely used way to validate imaging methods consists in inverse crime while the validity of applications on real dataset is conditioned by strong *a priori* and a
150 weak knowledge of the target. All of these leads to a limited validation of the efficiency imaging methods to recover parameter models. Thus, it is critical for 2D inversion of field data to accurately correct the geometrical spreading.

Point-source data can corrected from geometrical spreading using a simple two-steps signal processing: (1) convolving each trace by $\sqrt{t^{-1}}$, where t is the time, to correct the phase shift
155 of $\pi/4$ (2) applying a taper \sqrt{t} to all traces to correct amplitudes. Some variation exist, for examples, using a linear source wavelet estimation method to correct the phase (Bre-

taudeau et al., 2013) or applying an offset conditioning (Tran et al., 2013). To correct some biases of these methods, Forbriger et al. (2014) and Schafer et al. (2014) have introduced, and successfully applied to synthetic data, the *hybrid method*. In the *hybrid method* the
160 geometrical spreading correction is conditioned by: (1) the offset, (2) the knowledge of the wave propagation velocities in the medium and (3) a user defined ratio used to smoothly correct amplitudes from near to far offsets. The results are thus strongly dependent of user's *a priori* and attempts. However, this kind of signal corrections are valid only for two-dimensional (x, z) medias invariant along the y -axis.

165 In other cases, 3D data are corrected or process *on the fly*, or used as is in algorithm using a 2.5D approximation.

Thus, the missing step between purely numerical validation and real data applications can be the use of experimental line-source seismograms recorded under controlled conditions.

Here, we take advantage of the experimental framework to explore an alternative approach
170 specific to MUSC system. Figure 4 presents a schematic representation of the principle for this kind of experiment. Theoretically, the stack of all receiver with the same offset will results in a pseudo line-source response. Yet, to simplify the experiment, an other way is to consider only one receiver per offset, on a line perpendicular and centered to the defined line-source. All traces of each common receiver gather are then stacked together to
175 obtain the line-source response. In order to apply this protocol, we have to choose a line-source's length L sufficiently great to be assimilated to a cylindrical source and above all a suitable sampling interval Δs between each point-source constituting the pseudo line-source to ensure applicability of the *Huygen's principle*.

For this experiment, we choose an homogeneous block of *F50 pure* epoxy-resin (see table

180 1 for physical parameters) with dimensions $500 \times 504 \times 115$ mm ($x \times y \times z$). Given the material's properties, we choose $L = 240$ mm and $ds = 0.5$ mm which leads to 481 point-source locations. Four receiver positions have been selected: 45, 50, 55 and 60 mm offset perpendicular to the line-source. The source wavelet is a Ricker with a central frequency $f_0 = 100$ kHz. Each receiver is perpendicular to and centered on the line-source. For each
185 receiver position, all recorded traces are stacked together to obtain an equivalent two-dimensional line-source response.

We first apply this method using 2D and 3D numerical modeling for 3D point-source, 3D line-source and 2D cylindrical source with a complete acquisition of 120 receivers spaced of 1 mm and a minimum offset of 45 mm. For these experiments, we did not take into account the
190 quality factor Q . Figure 6a shows the comparison between point-source response (3D) and line-source response (2D). As expected, both amplitude and phase are different. Then, we applied the *hybrid method* (?) on the point-source response to obtain the equivalent line-source response. Figure 6b shows that the *hybird method* is able to produce equivalent line-source response with a good agreement.

195 To evaluate the efficiency of the method, experimental line-source responses will be compared to point-source and equivalent line-source responses using the cross-correlation coefficient (**cc**) and the root mean square (**rms**) ratio. These values are presented in table 2. **cc_{init}** and **rms_{init}** correspond to direct evaluation whereas **cc_{final}** corresponds to the best **cc** obtained and **rms_{final}** is the corresponding **rms**.

200 We now apply this method to experimental data on the equivalent real reduced-scale model. Figures 7(a) show the comparison between experimental traces obtained using a point-source and a line-source for source-receiver offsets 50, 55, 60 and 65 mm respectively. It

is straightforward that these waveforms are not similar in terms of both phases (**cc**<0.75) and amplitude (**rms**>0.4). Even after amplitude fitting, point-source response to the line-
 205 response in term of phase (**cc**<0.8), amplitudes do not match (**rms**>0.4). These results confirm that using raw point-source responses in a two-dimensional inversion process or imaging method can be critical in terms of convergence and validity of the results since these methods are built over phase and/or amplitude similarity.

Figures 7(b) show the comparison between experimental traces using a line-source and a
 210 point-source after geometrical spreading corrections (equivalent line-source response) using the same parameters than for numerical experiment. The cross-correlation coefficient **cc** for these waveforms are greater than 0.95 and rms<0.25. These results denote that the experimental line-source response is correct in terms of phase compared to an equivalent line-source response. However, **rms** are quite great even if they are smaller than previously.
 215 This can be explained by small differences in terms of waveforms and phases which are critical in the final **rms** results. Moreover, the *hybrid* method to obtain the equivalent line-source response from a point-source response needs accurate parametrization to obtain the best result which is not necessarily in a good agreement with the attempt true line-source response.

220 These results show that the line-source emulation on the MUSC system is efficient and can produce data suitable for imaging methods such as 2D FWI.

Experimental source reproducibility

We have shown the MUSC system is able to generate high quality 2D experimental seismograms. However, experimental data, as other, must be reproducible to be used as a

225 reference or in an inversion process. As shown by Bretaudeau et al. (2011), the source waveform injected in the reduced-scale model by the piezo-electric source is not similar to the selected theoretical one. Figure (?), of data recorded in an homogeneous model, shows clearly multiple wavefront following the main arrival. After Bretaudeau et al. (2011), these multiples are generated inside the conical adapter of the piezo-electric source.

230 To assess the ability of MUSC system to provide reproducible data, *i.e.* to evaluate the reproducibility of the source impact, several physical modeling were performed on the same homogeneous epoxy-resin block as in previous section.

Ten realizations have been acquired on this model with a similar geometry setup, *i.e.* 120 receivers positions with an increment equal to 1 mm and a minimum offset of 10 mm. The numerical wavelet sent to the piezoelectric transducer source is a Ricker signal with a central
235 frequency of 100 kHz. However, the source waveform is modified by the physical coupling effect of the transducer.

A mean shot gather, calculated from the ten experiments, is used as reference seismogram. Figure 9 shows the central trace of each realization and **cc** gives the correlation coefficient of
240 each trace with the reference one. The **cc** are always greater than 0.98 which demonstrate the very high reproducibility of data generated by the MUSC system.

In a second step, a unique source wavelet is estimated using a linear source wavelet estimation method based on a stabilized deconvolution (Pratt, 1999). The source wavelet estimation takes into account the ten experiments together and allows to obtain a mean
245 effective source suitable for each experiment. The resulting source wavelet is applied to the synthetic signals (figure 11). The corrected seismograms are in good agreement with the experimental seismograms (correlation coefficients > 0.96) confirms the great efficiency of

the wavelet source assessment process.

These last results, based on an average estimated source wavelet show that the effective
250 impulse source emitted by the transducer in the MUSC system measurement bench is
stable enough to ensure a robust reproducibility of the source. Therefore, concerning the
key issue of the source knowledge, experimental data acquired in the MUSC system can be
efficiently processed by imaging methods like Full Waveform Inversion (FWI) with only one
estimation step for all the multi-source and multi-receivers data.

255 However, this last result does not mean that the source will be the same for an experiment
for an other experiment on an other model. Thus, we consider now a more complex model,
called *BiAlt*. This model, shown in figure (???) is a two-layer model with a central alter-
ation. We generate synthetic seismogram with the 2D SEM algorithm and using the mean
effective source wavelet estimated on homogeneous block as a source function. Figure 13
260 shows that the synthetic seismogram using the effective source wavelet is in good agreement
with the experimental one...

This last result shows that the MUSC source is stable from an experiment to an other and
can be consequently injected as an input in modeling and imaging methods without any
pre-processing or *on the fly* source inversion.

CONCLUSIONS

265 These two studies allow to refine the capacity of the physical modeling designed for seismic
experiments simulation by 1) completing the validation of the measurement through com-
parison of numerical and experimental data generated by a realistic 2D source line and 2)
assessing the reproductivity of the effective source emitted in a model. These improvements

allow to provide and distribute experimental reduced scale data to the scientific community

270 as benchmark datasets.

PLOTS

Equations

Figures

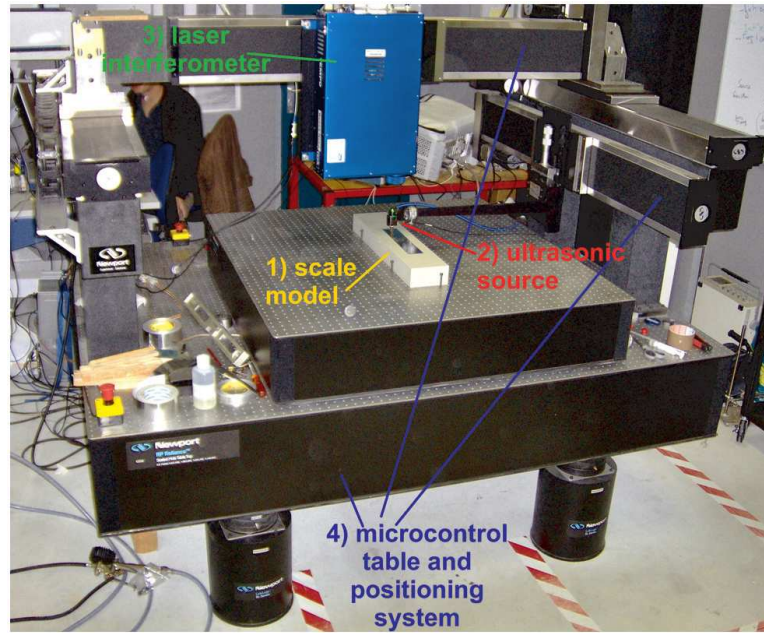


Figure 1: Photograph of the MUSC ultrasonic laboratory (from Bretaudeau et al. (2013)) with its four components: (1) a small-scale model of the underground, (2) an optical table with two automated arms moving above the model, (3) a laser interferometer recording ultrasonic wave propagation at the model surface, and (4) a piezoelectric ultrasonic source generating ultrasonic waves in the model.

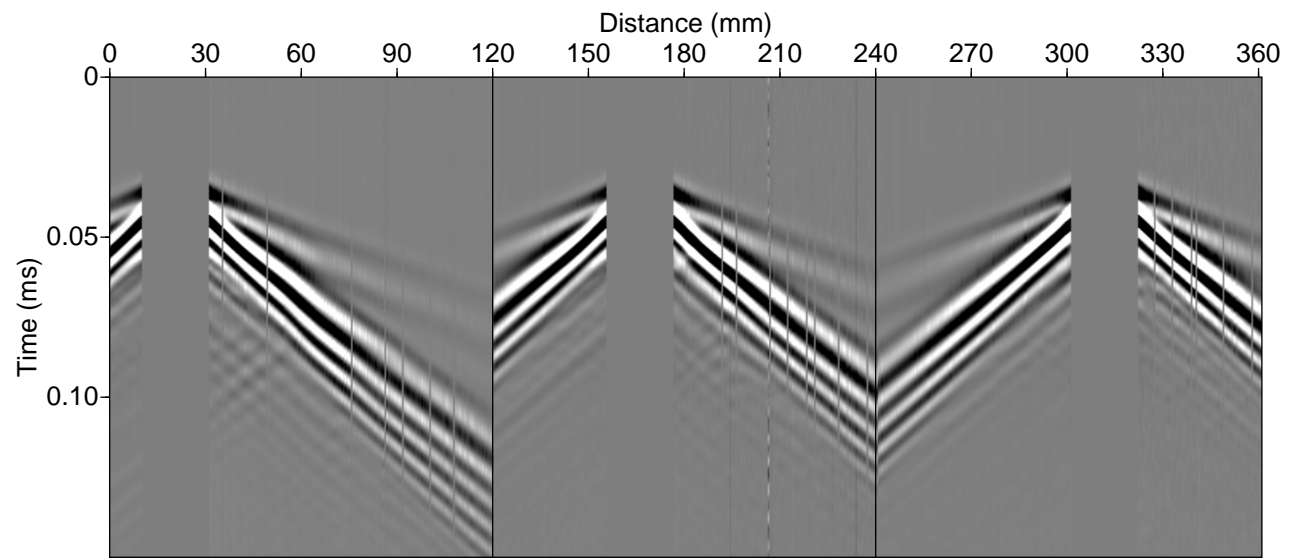


Figure 2: Example of multi-source multi-receiver record on the MUSC system for a two-layer model (balt).

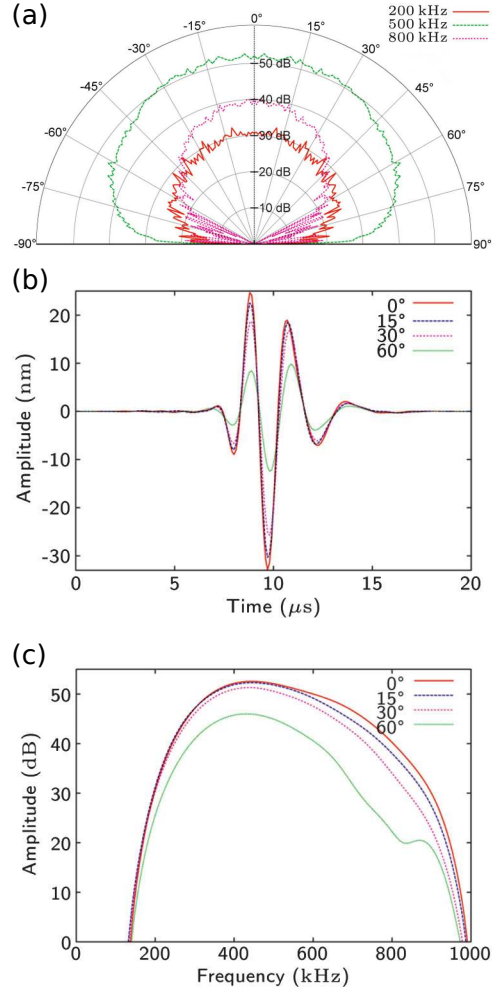


Figure 3: Validation of the piezoelectric source coupled with an adapter (Bretaudeau et al., 2011). (a) Directivity diagrams (dB) for the high-frequency source Panametrics® with conical polyurethane adapter: three frequencies normal particle displacement. (b) Temporal signals and (c) amplitude spectrums for the high-frequency source Panametrics® with a conical polyurethane adapter in transmission through a PVC cylinder for various angles of incidence: 0, 15, 30, and 60 degrees normal particle displacement.

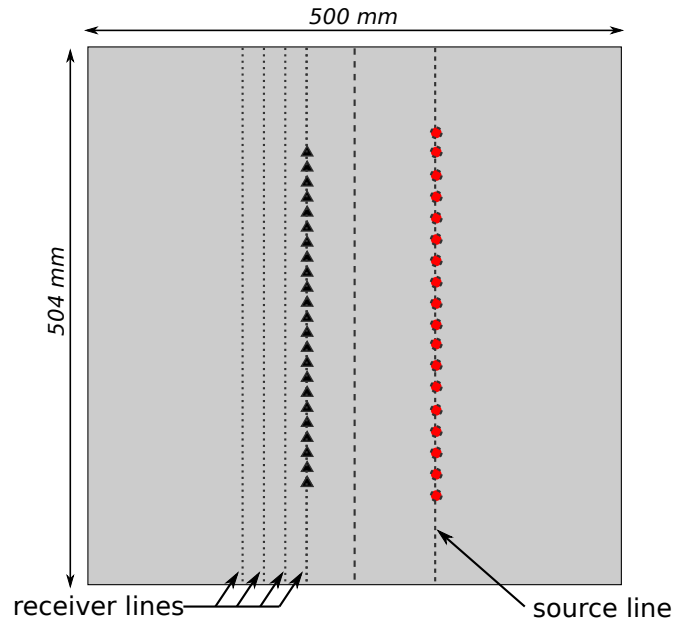


Figure 4: Schematic representation of the acquisition geometry used to generate experimental line-source, *i.e.* an equivalent of cylindrical source use in two-dimensional modeling. Black triangle and red circle represent receivers and sources, respectively.

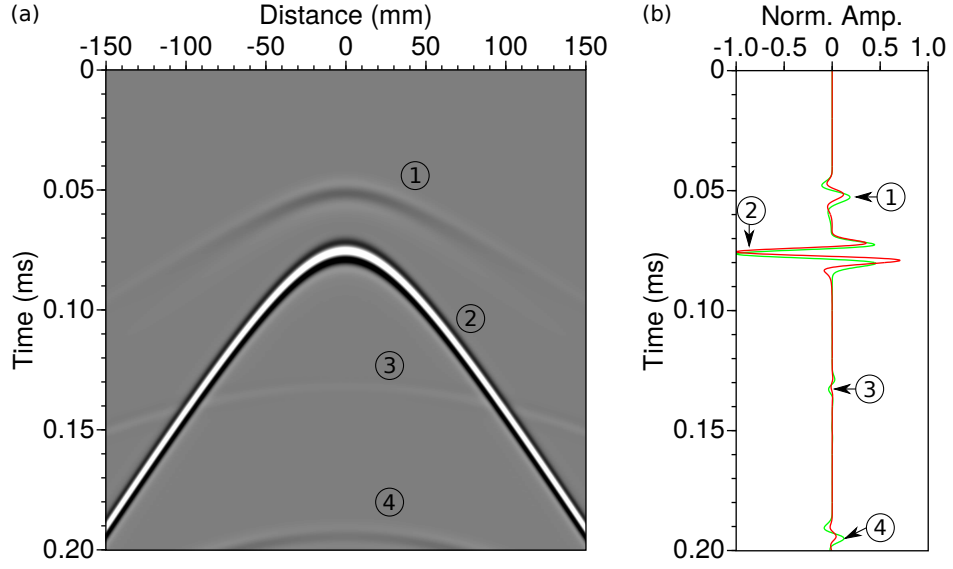


Figure 5: (a) Resulting seismogram at one receiver position for the experimental line-source. (b) Comparison between point-source response in red (central trace of (a)) and line-source response in green (stack of (a)). Some wavefront are pointed: (1) P-wave, (2) surface wave, (3) reflected PP and (4) reflected PSv -wave on the bottom of the model.

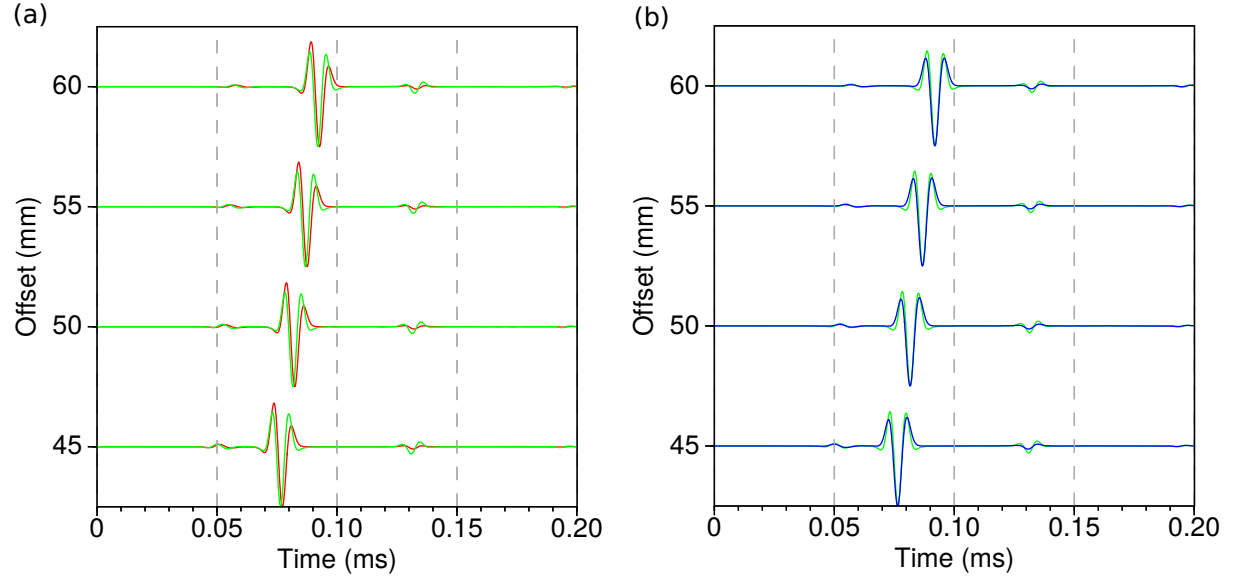


Figure 6: (a) Comparison between an experimental seismogram for a point-source (red) and for a line source (black), for 50, 55, 60 and 65 mm source-receiver offsets respectively. (b) Comparison between an experimental seismogram for a line-source (black), and a point-source response corrected from geometrical spreading (green) for same source-receiver offsets as (a). \mathbf{cc} gives the correlation factor between line-source and point-source responses.

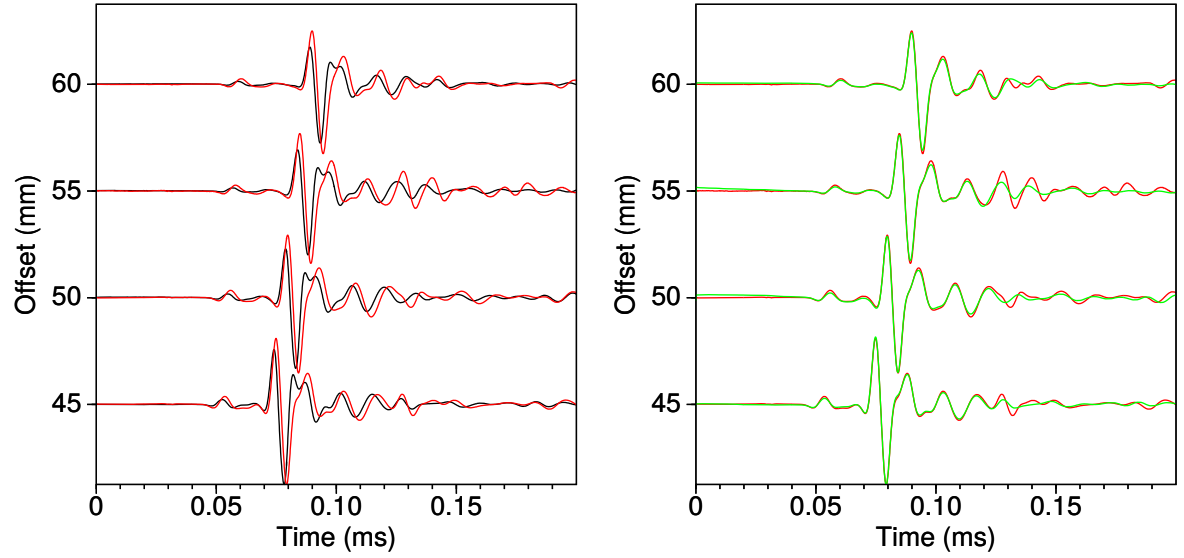


Figure 7: (a) Comparison between an experimental seismogram for a point-source (red) and for a line source (black), for 50, 55, 60 and 65 mm source-receiver offsets respectively. (b) Comparison between an experimental seismogram for a line-source (black), and a point-source response corrected from geometrical spreading (green) for same source-receiver offsets as (a). **cc** gives the correlation factor between line-source and point-source responses.

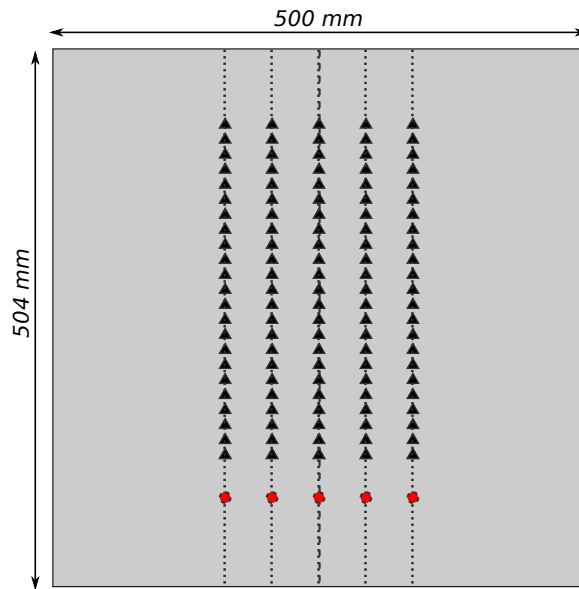


Figure 8: Schematic representation of the acquisition geometry used to assess the data reproducibility using the MUSC system. Black triangle and red circle represent receivers and sources, respectively.

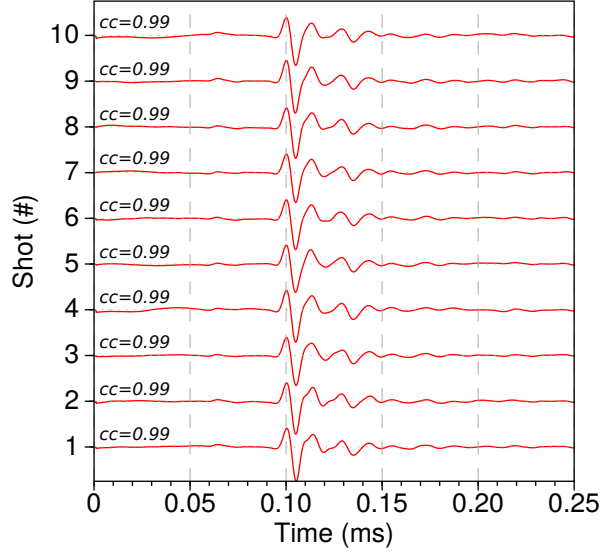


Figure 9: Central trace for each of the ten analogic experiment. `cc` gives the correlation factor of each central trace with respect to a mean trace.

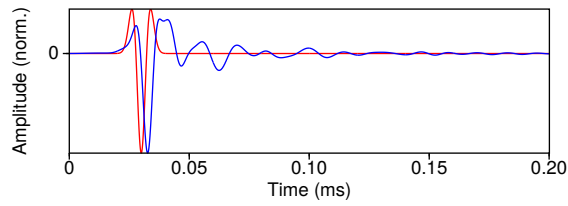


Figure 10: Comparison between the theoritical Ricker source send to the transducer and the effective source wavelet injected in the model.

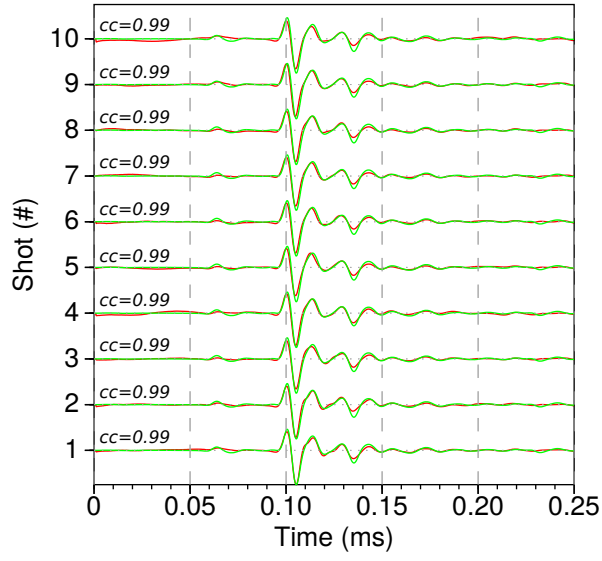


Figure 11: Comparison between analogic central traces (grey) and numerical traces corrected from the estimated effective source (black) for each experiment. cc gives the correlation coefficient.

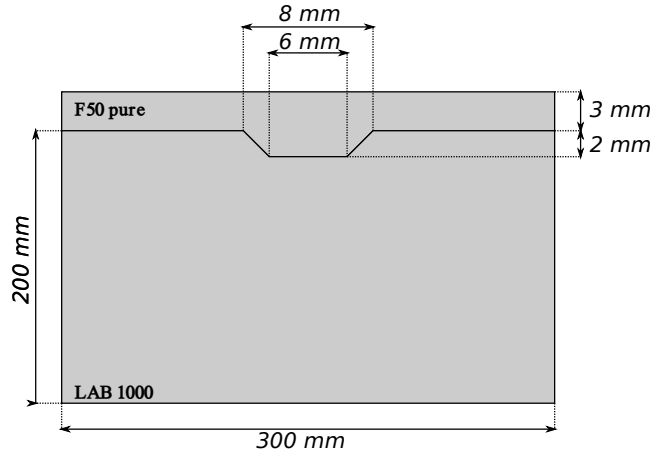


Figure 12: Schematic representation of the so-called *BiAlt* model.

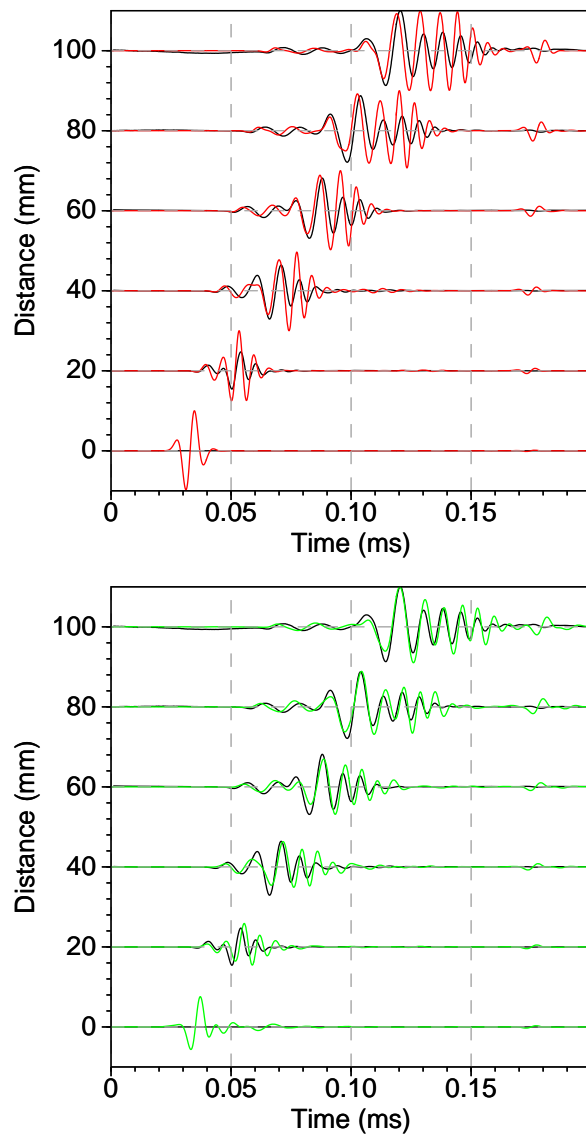


Figure 13: .

Tables

material	V_P (m/s)	V_S (m/s)	V_R (m/s)	ρ (kg/m ³)	Q
Aluminium	5630	3225	–	2700	–
F50 pure	2300	1030	965	1300	30
F50 200%	2820	1425	1328	1766	–
F50 240%	2968	1496	1388	1822	–
LAB1000	2850	1400	1310	1500	75

Table 1: Physical properties of some materials used to build small scale models. V_P , V_S and V_R are the P-wave velocity, S-wave and the Rayleigh wave velocity, respectively. ρ is the density and Q is the quality factor.

	90 mm	95 mm	100 mm	105 mm
$cc1_{init}$	0.702	0.725	0.728	0.728
$rms1_{init}$	0.794	0.760	0.762	0.774
$cc1_{final}$	0.940	0.953	0.951	0.949
$rms1_{final}$	0.358	0.317	0.325	0.343
$cc2_{init}$	0.954	0.987	0.988	0.988
$rms2_{init}$	0.304	0.162	0.155	0.154
$cc2_{final}$	—	—	—	—
$rms2_{final}$	—	—	—	—

Table 2: .

ACKNOWLEDGMENTS

REFERENCES

- Bérenger, J. P., 1994, A perfectly matched layer for the absorption of electromagnetic waves:
275 Journal of Computational Physics, **114**, 185–200.
- Berkhout, A., D. Verschuur, and G. Blacquiere, 2012, Illumination properties and imaging
promises of blended, multiple-scattering seismic data: a tutorial: Geophysical Prospecting,
60, 713–732.
- Bishop, T., K. Bube, R. Cutler, R. Langan, P. Love, J. Resnick, R. Shuey, and D. Spinder,
280 der, 1985, Tomographic determination of velocity and depth in laterally varying media:
Geophysics, **50**, 903–923.
- Bohm, G., J. M. Carcione, D. Gei, S. Picotti, and A. Michelini, 2015, Cross-well seismic
and electromagnetic tomography for CO₂ detection and monitoring in a saline aquifer:
Journal of Petroleum Science and Engineering, **133**, 245–257.
- 285 Bretaudeau, F., 2010, Modélisation physique à échelle réduite pour l’adaptation de
l’inversion des formes d’ondes sismiques au génie civil et à la subsurface: PhD thesis,
Université de Nantes.
- Bretaudeau, F., R. Brossier, D. Leparoux, O. Abraham, and J. Virieux, 2013, 2d elastic full-
waveform imaging of the near-surface: application to synthetic and physical modelling
290 data sets: Near Surface Geophysics.
- Bretaudeau, F., D. Leparoux, and O. Abraham, 2008, Small scale adaptation of the seismic
full waveform inversion method - application to civil engineering applications.: The
Journal of the Acoustical Society of America, **123**.
- Bretaudeau, F., D. Leparoux, O. Durand, and O. Abraham, 2011, Small-scale modeling of
295 onshore seismic experiment: A tool to validate numerical modeling and seismic imaging
methods: Geophysics, **76(5)**, T101–T112.

- Cristini, P., and D. Komatitsch, 2012, Some illustrative examples of the use of the spectral-element method in ocean acoustics.: *Journal of the Acoustical Society of America*.
- Favretto-Cristini, N., A. Tantsereva, P. Cristini, B. Ursin, D. Komatitsch, and A. Aizenberg, 2013, Numerical modeling of zero-offset laboratory data in a strong topographic environment: results for a spectral-element method and a discretized kirchhoff integral method: *Earthquake Science*.
- Festa, G., and J. Vilotte, 2005, The Newmark as velocity-stress time-staggering: an efficient PML implementation for spectral element ssimulation of elastodynamics: *Geophysical Journal International*, **161**, 798–812.
- Forbriger, T., L. Gross, and M. Schafer, 2014, Line-source simulation for shallow-seismic data. part 1: theoretical background: *Geophysical Journal International*, **198**, 1387–1404.
- French, W. S., 1974, Two-dimensional and three-dimensional migration of model-experiment reflection profiles: *Geophysics*, **39(3)**, 265–277.
- Geuzaine, C., and J. Remacle, 2009, Gmsh: a three-dimensional finite element mesh generator with built-in pre- and post-processing facilities.: *International Journal for Numerical Methods in Engineering*, **79**, 1309–1331.
- Guofeng, L., L. Yaning, R. Li, and M. Xiaohong, 2013, 3d seismic reverse time migration on gpgpu: *Computers & Geosciences*, **59**, 10–23.
- Hilterman, F., 1970, Three-dimensional seismic modeling: *Geophysics*, **35**, 1020–1037.
- Howes, E., L. Tejada-Flores, and L. Randolph, 1953, Seismic model study: *Journal of the Acoustical Society of America*, **25**, 915–921.
- Hulbert, G. M., and T. J. Hughes, 1990, Space-time finite element methods for second-order hyperbolic equations: *Computer Methods in Applied Mechanics and Engineering*, **84**, 327–348.

- Isaac, J. H., and D. C. Lawton, 1999, Image mispositioning due to dipping media: A physical seismic modeling study: *Geophysics*, **64**, 1230–1238.
- Karniadakis, G. E., 1989, Spectral element simulations of laminar and turbulent flows in complex geometries: *Applied Numerical Mathematics*, **6**, 85 – 105. (Special Issue on Spectral Multi-Domain Methods).
- Komatitsch, D., and J. Tromp, 1999, Introduction to the spectral-element method for three-dimensional seismic wave propagation: *Geophysical Journal International*, **139**, 806–822.
- Komatitsch, D., S. Tsuboi, and J. Tromp, 2005, The spectral-element method in seismology.
- Komatitsch, D., J. P. Vilotte, R. Vai, J. M. Castillo-Covarrubias, and F. J. Sánchez-Sesma, 1998, The Spectral Element Method for Elastic Wave Equation: Application to 2-D and 3-D Seismic Problems: *International Journal for Numerical Methods in Engineering*, **45**, 1139–1164.
- Korczak, K. Z., and A. T. Patera, 1986, An isoparametric spectral element method for solution of the navier-stokes equations in complex geometry: *Journal of Computational Physics*, **62**, 361 – 382.
- Levander, A., 1988, Fourth-order finite-difference p-sv seismograms: *Geophysics*, **53**, 1425–1436.
- Lysmer, J., and L. A. Drake, 1972, A finite element method for seismology: *Methods in computational physics*, **11**, 181–216.
- Moczo, P., J. Kristek, and L. Halada, 2004, The finite-differences method for seismologists: An introduction: Comenius University, Bratislava.
- Morozov, I., 2004, Crustal scattering and some artefacts in receiver function images: *Bulletin of the Seismological Society of America*, **94**, 1492–1499.
- Patera, A. T., 1984, A spectral element method for fluid dynamics: Laminar flow in a

- 345 channel expansion: *Journal of Computational Physics*, **54**, 468–488.
- Perez Solano, C., D. Donno, and H. Chauris, 2014, Alternative waveform inversion for surface wave analysis in 2-d media: *Geophysical Journal International*, **198**, 1359–1372.
- Pratt, R. G., 1990, Frequency domain elastic wave modeling by finite differences: A tool for cross-hole seismic imaging.: *Geophysics*, **55**, 626–632.
- 350 ———, 1999, Seismic waveform inversion in the frequency domain, Part 1: Theory and verification in a physical scale model: *Geophysics*, **64**, 888–901.
- Rieber, F., 1936, Visual presentation of elastic wave patterns under various structural conditions: *Geophysics*, **1**, 196–218.
- Robertsson, J., J. Blanch, and W. Symes, 1994, Viscoelastic finite-difference modeling.: *Geophysics*, **59**, 1444–1456.
- 355 Saenger, E. H., and T. Bohlen, 2004, Finite-difference modeling of viscoelastic and anisotropic wave propagation using the rotated staggered grid: *Geophysics*, **69**, 583–591.
- Saenger, E. H., N. Gold, and A. Shapiro, 2000, Modeling the propagation of elastic waves using a modified finite-difference grid: *Wave Motion*, **31**, 77–92.
- 360 Sarkar, D., A. Bakulin, and R. L. Kranz, 2003, Anisotropic inversion of seismic data for stressed media: Theory and a physical modeling study on berea sandstone: *Geophysics*, **68**, 1–15.
- Schafer, M., L. Gross, T. Forbriger, and T. Bohlen, 2014, Line-source simulation for shallow-seismic data. part2: full-waveform inversion – a synthetic 2-d case study: *Geophysical Journal International*, **198**, 1405–1418.
- 365 Seron, F. J., F. J. Sanz, M. Kindelan, and J. I. Badal, 1990, Finite-element method for elastic wave propagation: *Communications in applied numerical methods*, **6**, 359–368.
- Stekl, I., and R. G. Pratt, 1998, Accurate visco-elastic modeling by frequency-domain finite

- differences, using rotated operators.: *Geophysics*, **63**, 1779–1794.
- 370 Tran, K. T., M. McVay, M. Faraone, and D. Horhota, 2013, Sinkhole detection using 2d
full seismic waveform tomography: *Geophysics*, **78**, R175–R183.
- Tromp, J., D. Komatitsch, and Q. Liu, 2008, Spectral-element and adjoint methods in
seismology.: *Commun Comput Phys*.
- Virieux, J., 1986, P-sv wave propagation in heterogeneous media: velocity-stress finite-
375 difference method: *Geophysics*, **51**, 889–901.
- Virieux, J., and S. Operto, 2009, An overview of full-waveform inversion in exploration
geophysics: *Geophysics*, **74**, WCC1WCC26.
- Wirgin, A., 2004, The inverse crime: *ArXiv Mathematical Physics e-prints*. (Provided by
the SAO/NASA Astrophysics Data System).
- 380 Wong, J., K. W. Hall, E. V. Gallant, R. Maier, M. Bertram, and D. C. Lawton, 2009,
Seismic physical modeling at university of calgary: *CSEG recorder*, **34**.